JACS Au
AN OPEN ACCESS JOURNAL OF THE AMERICAN CHEMICAL SOCIETY

pubs.acs.org/jacsau

Article

Unexpected Disparity in Photoinduced Reactions of C_{60} and C_{70} in Water with the Generation of $O_2^{\bullet-}$ or $^1O_2$

Korinne Liosi, Anton J. Stasyuk, Fabio Masero, Alexander A. Voityuk, Thomas Nauser, Victor Mougel,* Miquel Solà,* and Yoko Yamakoshi*

Cite This: *JACS Au* 2021, 1, 1601−1611

Read Online

ACCESS | Metrics & More | Article Recommendations | Supporting Information

ABSTRACT: Well-defined fullerene-PEG conjugates, C_{60}-PEG (**1**) and two C_{70}-PEG (**2** and **3** with the addition sites on *ab*-[6,6] and *cc*-[6,6]-junctions), were prepared from their corresponding Prato monoadduct precursors. The resulting highly water-soluble fullerene-PEG conjugates **1**−**3** were evaluated for their DNA-cleaving activities and reactive oxygen species (ROS) generation under visible light irradiation. Unexpectedly, photoinduced cleavage of DNA by C_{60}-PEG **1** was much higher than that by C_{70}-PEG **2** and **3** with higher absorption intensity, especially in the presence of an electron donor (NADH). The preference of photoinduced ROS generation from fullerene-PEG conjugates **1**−**3** via the *type II* (energy transfer) or the *type I* (electron transfer) photoreaction was found to be dependent on the fullerene core (between C_{60} and C_{70}) and functionalization pattern of C_{70} (between **2** and **3**). This was clearly supported by the electron transfer rate obtained from cyclic voltammetry data and computationally estimated relative rate of each step of the *type II* and the *type I* reactions, with the finding that *type II* energy transfer reactions occurred in the inverted Marcus regime while *type I* electron transfer reactions proceeded in the normal Marcus regime. This finding on the disparity in the pathways of photoinduced reactions (*type I* versus *type II*) provides insights into the behavior of photosensitizers in water and the design of photodynamic therapy drugs.

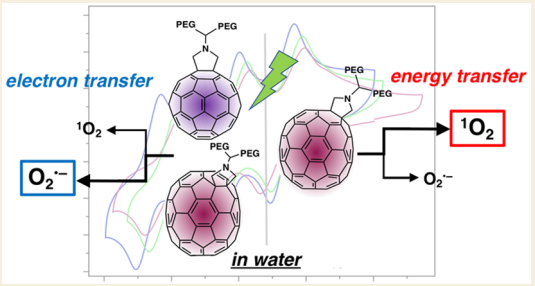

KEYWORDS: *water-soluble fullerene, reactive oxygen species, photoinduced electron transfer, photoinduced energy transfer, photosensitizer, photodynamic therapy*

INTRODUCTION

Applications of fullerenes (C_{60} and C_{70}) as photosensitizers (PSs) in photodynamic therapy (PDT) have been considered for decades.[1−3] Fullerenes offer suitable photophysical properties as PDT-PSs: (1) they generate reactive oxygen species (ROS) in high quantum yields (e.g., quantitative singlet oxygen ($^1O_2$) in organic solvents)[4−6] and (2) they can be excited by light with low-energy in the vis-NIR region, which can penetrate deeper into tissues, while being less harmful. In addition, there is no significant toxicity reported for C_{60} and C_{70} in the absence of light. Among fullerenes, C_{70} has been regarded as an excellent PDT-PS since it shows relatively higher absorption intensity than C_{60} in the visible region. Furthermore, its triplet excited state has a longer lifetime (τ > 2.2 ms in benzene and 51 ms in toluene) in comparison to C_{60} (133 μs and 0.41 ms, respectively).[7,8] Indeed, C_{70} acts as a good photocatalyst for generating $^1O_2$ that affects oxidations under visible light irradiation in $CHCl_3$.[9]

The understanding of the mechanism for the generation of ROS is key to rationally improving PSs for PDT applications. The generation of ROS from fullerenes was found to proceed mainly via two pathways (*type II* energy transfer and *type I* electron transfer, Scheme 1). The *type II* energy transfer pathway was reported by Foote and co-workers for both C_{60} and C_{70} in organic solvents and observed as the quantitative generation of $^1O_2$.[4,5] Almost simultaneously, *type I* electron transfer was reported by Kursic et al. and Foote et al.,[10,11] based on the calculated redox potential of the triplet excited state of C_{60} ($^3C_{60}$*), which was higher than that in its singlet

Scheme 1. Photoinduced Reactive Oxygen Species Generation from Fullerenes (n = 30, 35)

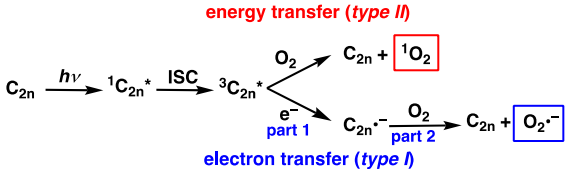

Received: May 28, 2021
Published: August 10, 2021

ground state ($^1C_{60}$: E_1 = −0.42 V vs SCE in PhCN; $^3C_{60}$*: E_1 = +1.14 V vs SCE in PhCN). Via this *type I* pathway, the generation of $O_2^{\bullet-}$ and $^\bullet$OH was observed in aqueous solution of C_{60} complexed with poly(vinylpyrrolidone) (C_{60}/PVP) using electron spin resonance (ESR) spin-trapping methods, while no $^1O_2$ generation was observed.[12,13] However, the detailed mechanism of the photoinduced ROS generation from fullerenes in water remains unclear.[14] Such mechanism can vary depending on the structures of water-soluble fullerene materials prepared by complexation and derivatization.[2,15,16] In particular, ROS generation from photoexcited C_{70} in aqueous media has not been well-described yet.

Beyond the recent report by the Hamblin group that cationic C_{70} derivatives can be used as PDT-PS that showed photocytotoxicity to cancer cell lines[17] and photodynamic antimicrobial activity,[18] C_{70} derivatives have not been extensively investigated for PDT applications. This paucity of studies results from the complex generation of multiple C_{70} isomers upon derivatization. Even simple monoderivatization methods such as Diels−Alder cycloadditions[19] or 1,3-dipolar cycloaddition reactions (Prato reaction)[20] applied to C_{70} produced several isomers (*ab*-[6,6], *cc*-[6,6], and *de*-[6,6] or *dd*-[5,6]), while C_{60} usually generates just one [6,6]-isomer due to the higher double bond character of the [6,6]-bond and I_h symmetry of C_{60}.[21] Such changes in the addition patterns in fullerenes often induce differences in their UV−vis absorption spectra affecting their photophysical properties, especially in ROS generation. Indeed, there were several previous reports on the differences in photophysical properties of C_{70} isomers.[22,23] The investigation of the photophysical properties of isolated isomers of C_{70} derivatives is important for advancing their PDT applications.

In this study, we used well-defined, water-soluble C_{60}-PEG **1**[24] and C_{70}-PEG derivatives **2** and **3**,[20] and tested them for photoinduced DNA damage. The generation of ROS ($^1O_2$ and $O_2^{\bullet-}$) in conjugates **1**−**3** was measured by ESR in the presence of spin-trapping agents. These results revealed unexpected disparities in both DNA cleavage and the ROS generation ($^1O_2$ versus $O_2^{\bullet-}$) between these conjugates **1**−**3**. To understand these differences, photophysical (laser flash photolysis) and electrochemical (cyclic voltammetry) measurements were performed. Finally, computational studies were employed to investigate the reaction rate of each step in *type II* and *type I* pathways to understand the mechanisms of ROS generation from C_{60}-PEG and C_{70}-PEG conjugates **1**−**3**.

EXPERIMENTAL SECTION

General

NMR spectra were recorded at room temperature on Bruker 400 spectrometer and Bruker 600 spectrometer equipped with a CryoProbe (Bruker BioSpin GmbH). HRMS spectra were recorded on a Bruker MALDI-TOF, Bruker maXis ESI-QTOF spectrometer, and Bruker solariX spectrometer (Bruker Daltonics GmbH). FT-IR spectra were recorded on PerkinElmer Spectrum One FT-IR spectrometer with a universal ATR sampling accessory (PerkinElmer Inc.). HPLC analyses were carried out using JASCO PU-2080 Plus HPLC pump, JASCO MD2018 Plus detector, and ChromNAV chromatography data system (JASCO, Co.). UV−vis spectra were recorded on Varian Cary 500 Scan UV−vis NIR Spectrophotometer (Varian Inc.). Column chromatography and analytical TLC were performed on SilicaFlash F60 (230−400 mesh) (SiliCycle Inc.) and silica gel 60 F254 TLC (Merck KGaA), respectively. All the solvents used were HPLC grade and purchased from Acros Organic (Thermo Fischer Scientific, Inc.). All used water were Milli-Q water.

Synthesis of Water-Soluble C_{60}-PEG 1 and C_{70}-PEG 2 and 3 Conjugates

The bis-carboxylic acid ester precursors for C_{60} and C_{70} were prepared by reported methods.[20,25] Obtained [6,6]-adduct of C_{60} (**4**) and *ab*-[6,6]- and *cc*-[6,6]-adducts of C_{70} (**5**, **6**) were converted to C_{60}-PEG **1**[24] and C_{70}-PEG **2**, **3** by deprotection and subsequent conjugation with amino-PEG_{36}-^{t}Bu ester (Scheme S1). **2**: ^{1}H NMR (600 MHz, in $CDCl_3$) δ_H 1.44 (s, $(CH_3)_3$, 18H), 2.49 (t, J = 6.6 Hz, $CH_2-CH_2-CO_2$-^{t}Bu, 4H), 3.62−3.65 (CH_2-CH_2-O, 298H); ^{13}C NMR (150 MHz, in $CDCl_3$) δ_C 28.1 ($C(CH_3)_3$), 36.3 ($CH_2-CH_2-CO_2$-^{t}Bu), 39.2 ($CH-CH_2-CO-NH$), 39.9 ($CH_2-CH_2-NH-CO$), 54.6 ($(CH_2)_2-CH-N$), 59.1 ($C-CH_2-N$), 61.3 ($C-CH_2-N$), 63.0 ($C-CH_2-N$), 63.2 ($C-CH_2-N$), 66.9 ($O-CH_2-CH_2-CO_2$-^{t}Bu), 70.5 (CH_2-CH_2-O), 80.5 ($C(CH_3)_3$), 131.2, 131.3, 131.6, 133.7, 133.8, 137.4, 140.5, 140.6, 142.8, 143.2, 143.3, 145.8, 146.3, 146.7, 146.9, 147.0, 147.1, 147.1, 147.4, 148.8, 149.1, 149.4, 149.5, 149.7, 149.9, 150.2, 150.7, 150.8, 151.0, 151.2, 151.4, 151.4, 155.6 158.1, 170.9; HRMS (MALDI/ESI), matrix: CCA + NA-PFHA) m/z calcd for $[C_{235}H_{325}NaN_3O_{78}]^+$: 4460.1449, found 4460.1470 ($[M + Na]^+$). **3**: ^{1}H NMR (600 MHz, $CDCl_3$) δ_H 1.44 (s, $(CH_3)_3$, 18H), 2.49 (t, J = 6.6 Hz, $CH_2-CH_2-CO_2$-^{t}Bu, 4H), 3.62−3.67 (m, CH_2-CH_2-O, 298H); ^{13}C NMR (150 MHz, $CDCl_3$) δ_C 28.3 ($C(CH_3)_3$), 36.4 ($CH_2-CH_2-CO_2$-^{t}Bu), 38.5 ($CH-CH_2-CO-NH$), 39.4 ($CH_2-CH_2-NH-CO$), 59.6 ($C-CH_2-N$), 62.4 ($C-CH_2-N$), 67.1 ($O-CH_2-CH_2-CO_2$-^{t}Bu), 70.7 (CH_2-CH_2-O), 80.7 ($C(CH_3)_3$), 126.2, 130.9, 131.5, 131.5, 132.2, 132.5, 141.0, 142.0, 142.7, 144.0, 144.4, 144.6, 144.7, 145.0, 145.4, 145.5, 146.1, 146.2, 146.2, 146.8, 146.9, 147.0, 147.3, 147.3, 147.4, 147.5, 148.1, 148.1, 148.3, 148.4, 149.1, 149.2, 149.3, 149.5, 150.1, 150.7, 150.7, 151.8, 153.0, 154.8, 171.1 (CH_2-CO_2-^{t}Bu); HRMS (MALDI/ESI, matrix: CCA + NA-PFHA) m/z calcd for $[C_{235}H_{325}NaN_3O_{78}]^+$: 4460.1449, found 4460.1515 ($[M + Na]^+$).

DLS Measurement

Dynamic light scattering (DLS) measurements were performed with an aqueous solution (1.0 mM) of each **1**, **2**, or **3** at room temperature on a Malvern Nano-Zeta Sizer (Malvern Instruments Ltd.).

STEM Analyses

Transmission electron microscopy (TEM) images were acquired on a Talos F200X (Thermo Fischer Scientific) instrument operated at 200 kV of accelerating potential in scanning TEM (STEM) mode.

DNA Cleavage Assay

Supercoiled plasmid pBR322 DNA (New England BioLabs) was used as a substrate. To a solution of pBR322 (12.5 $\mu g \cdot mL^{-1}$, 10 μL) in 10 mM Tris-HCl buffer (pH 8.0, with 1 mM EDTA), the aqueous solutions of **1**, **2**, or **3** (final conc.: 0.75 mM) and NADH (final conc.: 10 mM) were added (total volume: 20 μL) and subjected to photoirradiation by a green LED (Lumitronix ConextPlay, male grün, 5 V, 528 nm, 90 $lm \cdot W^{-1}$) with a distance of 1 cm for 6 h. Subsequently, an aliquot of glycerol solution of bromophenol blue (0.1%, 5 μL) was added subjected to agarose gel electrophoresis (1% agarose in Tris-borate-EDTA (TBE) buffer) in TBE buffer at 100 V for 80 min. The gel was stained with ethidium bromide and visualized by using a transilluminator (Vilber Lourmat Sté) and analyzed by ImageJ.

Detection of ROS Generations by ESR with Spin-Trapping Reagents

ESR spectra were recorded on a Bruker spectrometer (Bruker BioSpin, GmbH) equipped with microwave bridge X-band ESR. Diethylenetriaminepentaacetic acid (DETAPAC), NADH, 2,2,6,6-tetramethyl-4-piperidone (4-oxo-TEMP), and L-histidine were purchased from Sigma-Aldrich Co. Dimethyl sulfoxide (DMSO) was purchased from VWR Internationals, and 5-(diethoxyphosphoryl)-5-methyl-1-pyrroline-*N*-oxide (DEPMPO) was purchased from Enzo Life Sciences Inc. For the measurements of $^1O_2$ generation, C_{2n}-PEG **1**−**3** (40 μM) and 4-oxo-TEMP (80 mM) were mixed in 60 mM phosphate buffer (pH 7.0). For the measurements of $O_2^{\bullet-}$ generation, C_{2n}-PEG **1**−**3** (40 μM), DEPMPO (113 mM), NADH (10 mM), and

https://doi.org/10.1021/jacsau.1c00239
JACS Au 2021, 1, 1601−1611

DETAPAC (1 mM) were mixed in 60 mM phosphate buffer (pH 7.0) with 20% (v/v) DMSO in the presence or absence of L-histidine (10 mM). Each mixture above was irradiated with a green LED (Lumitronix, PowerBar V3, 528 nm, 93 lm·W^{-1}, with a total of 160 lamps assembled in a cylindrical manner with a distance of 4 cm, details are in the Supporting Information).

ESR measurements were carried out in a glass capillary (50 μL micropipet, Blaubrand), which was placed inside a thin-wall precision quartz ESR tube (Wilmad, Φ 4 mm × 250 mm). Double integration of ESR spectra was performed with the WiNEPR Processing program (Bruker). Measurement conditions: temperature 296 K, microwave frequency 9.78 GHz, microwave power 10 mW, receiver gain 5.0 × 10^4, modulation amplitude 1.00 G, modulation frequency 100 kHz, and sweep time 83.89 s.

Laser Flash Photolysis (LFP)

LFP experiments were carried out on an Applied Photophysics LKS 50 instrument. The solutions were transferred into quartz cuvettes that were sealed by a Young-type valve. Deaeration was carried out by repeated evacuation and flushing with argon. As an excitation laser, the second (532 nm) or the third harmonic (355 nm) of a Nd:YAG-Laser (Quantel Brilliant B) was used. C_{60}-PEG **1** was excited at 532 nm with energies of 20−50 mJ/pulse, C_{70}-PEG **2**, **3** were excited at 355 nm with energies of 40−90 mJ/pulse. Ten experiments were averaged per kinetics trace since the measured absorbance differences were very low for C_{70}-PEG **2** and **3**.

Cyclic Voltammetry

All measurements were performed under strictly anaerobic conditions in a conventional three electrode single-compartment cell with an SP300 Bio-Logic potentiostat (Bio-Logic Science Instruments SAS). A Ag/AgCl (Ag/AgCl glue in 0.1 M $TBAPF_6$/MeCN) reference electrode was used for the experimental setup. The reference electrode was placed in a compartment separated by a Vycor frit. All potentials were referred to internal Fc/Fc$^+$ standard added in the last step of the experiments. Three mm diameter glassy carbon electrodes (GCE, BASi) were used as working electrodes. Electrodes were polished on a wet polishing cloth using a 1 μm diamond suspension before each use. The scan rate was 100 mV·s^{-1} unless otherwise noted. The half-wave potentials ($E_{1/2}$) were defined as the weighted average of the corresponding E_c (the potential at which highest current was achieved for a particular cathodic event) and E_a (the potential at which highest current for corresponding anodic process was achieved). Unless otherwise noted, 1 mM solutions in toluene−MeCN (10.4:1) containing 0.1 M $TBAPF_6$ as supporting electrolyte were used. For all CV data, the second of three successive scans was presented.

Computational Details

Geometry optimizations were performed employing the range-separated functional from Handy and co-workers' CAM-B3LYP[26] and Ahlrichs and Weigend's Def2-SVP basis set.[27] The empirical dispersion D3 correction with Becke−Johnson damping was employed.[28−30] Vertical excitation energies were calculated with the same functional and basis set using the Tamm−Dancoff approximation (TDA).[31] This method was proven to give accurate results for charge transfer processes involving fullerenes.[32] Solvent effects were estimated using a COSMO-like polarizable continuum model[33,34] in monopole approximation considering water as solvent. All calculations were performed with the Gaussian 16 (rev. A03) suite of programs.[35] Full computational details including how species **1**−**3** and NADH were modeled can be found in the Supporting Information.

RESULTS AND DISCUSSION

Preparation of Water-Soluble C_{60}-PEG and C_{70}-PEG Conjugates

The water-soluble C_{60}-PEG **1** and C_{70}-PEG **2**, **3** (Figure 1a) were prepared by the conjugation of amino-PEG_{36}-^{t}Bu ester with the C_{60} and C_{70} bis-carboxylic acid precursors (**4**−**6**) using hexafluorophosphate benzotriazole tetramethyl uronium (HBTU) as a coupling reagent (Scheme S1).[20,24,25] The C_{60}- and C_{70}-PEG (**1**−**3**) were purified by reversed phase HPLC and were thoroughly soluble in water (>5 mM). The UV−vis-NIR spectra of C_{2n}-PEG (**1**−**3**) in water (Figure 1b) shows that all **1**−**3** had the absorption in the range of the phototherapeutic window (650−860 nm), with a much higher intensity for C_{70}-PEG **2**, **3** in comparison to C_{60}-PEG **1**. Computational results reproduce this experimentally observed trend (Figure S14). Compared to the spectra of pristine C_{60} and C_{70}, and precursors **4**−**6** measured in $CHCl_3$, aqueous solutions of **1**−**3** revealed relatively red-shifted spectra (Figure S13). Similar to the observed situation in precursors **5** and **6**, different absorption patterns were found between two isomeric C_{70}-PEG **2** and **3** in the visible region.[28] The observed longest absorption bands for **1**−**3** were respectively at ca. 720, 680, and 715 nm (inset of Figure 1b). The absorption intensities of **1**−**3** at 528 nm (maximum wavelength of green LED light, used in a later section) were found to have molar absorption coefficients (ε) of 2570, 14 600, and 10 200 M^{-1}·cm^{-1}, in line with the theoretical calculation results with an absorbance ca. 1.5 times higher for our computed model of **2** than for our computed model of **3** (Figure S14).

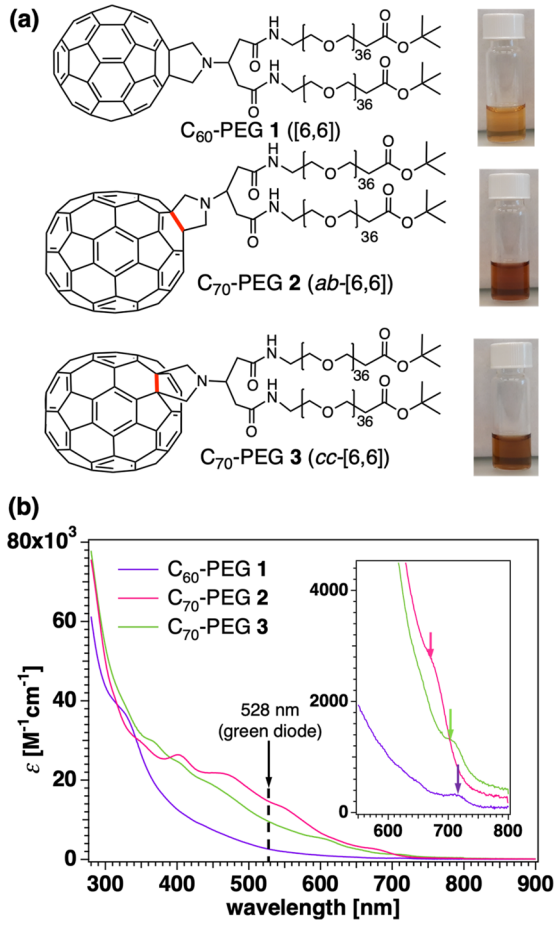

Figure 1. (a) Structures of C_{60}-PEG **1** and C_{70}-PEG **2**-**3** conjugates and their aqueous solutions (b) UV−vis spectra in water with expansion (inset). ε = 2570, 14 600, and 10 200 M^{-1}·cm^{-1} at 528 nm for **1**, **2**, and **3**.

https://doi.org/10.1021/jacsau.1c00239
JACS Au 2021, 1, 1601−1611

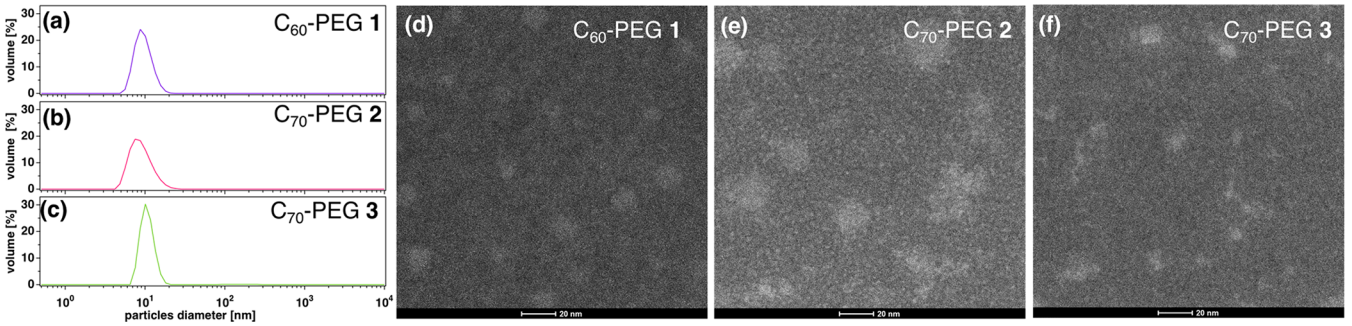

Figure 2. (a–c) DLS in volume distribution of C_{60}-PEG **1** (a), C_{70}-PEG **2** (b), and C_{70}-PEG **3** (c) in aqueous solution (1.0 mM). Mean (width) [nm]: (a) 9.57 (3.0), (b) 8.87 (3.4), and (c) 10.67 (2.8). (d–f) STEM images of C_{60}-PEG **1** (d), C_{70}-PEG **2** (e), and C_{70}-PEG **3** (f) in aqueous solution (0.2 mM).

Morphology Analyses by DLS and STEM

The combination of hydrophilic functionalizing groups and the hydrophobic fullerene surface may result in amphiphilic properties of compounds **1**–**3**. These compounds are hence expected to form micelle-type aggregates in water, which were confirmed in the previous study on compound **1** by surface tension measurements.[24] To study their assembly pattern, DLS measurements and STEM imaging were employed. The DLS results in water showed that the conjugates **1**–**3** were dispersed well in water by forming aggregates with mean diameters of ca. 9–11 nm with a single mode distribution (Figure 2a–c). It is known that the estimated length of the PEG_{36} chain used in this study was, in a linear form, approximately 13.4 nm in the all-*anti* conformation and 9.2 nm in the all-*gauche* conformation.[24] The hydrodynamic diameters of particles of compounds **1**–**3** (ca. 10 nm mean) observed by DLS suggested that the PEG moieties in the micelle-type aggregations of **1**–**3** are tangled (Figure S15).[36]

The STEM images of **1**–**3** (ca. 0.2 mM in water) were measured to obtain the morphological information on **1**–**3** in water. As shown in Figure 2d–f (and Figures S16–S18), all samples showed spherical-type aggregates, supporting their micelle-type assembly. While C_{60}-PEG **1** formed relatively more uniform and round morphologies, C_{70}-PEG **2** and **3** appeared to be rather random. Diameter analyses of the aggregates of the compounds **1**–**3** provided the mean in the range of 13–17 nm, in a good agreement to the DLS results (Figure S19).

Photoinduced DNA Cleavage

To preliminarily evaluate the efficiency of C_{60}-PEG and C_{70}-PEG **1**–**3** as PSs for PDT, photoinduced DNA cleavage tests were performed using a standard DNA (supercoiled pBR322) to quantify the formed nicked DNA (*form II*) in comparison to the intact ones (*form I*). A green diode with intensity maximum at 528 nm was used as a light source and photoirradiation was carried out for 6 h in the absence or the presence of an electron donor (NADH).

Results are shown in Figure 3. Sufficient DNA cleavage by **1**–**3** was observed (lanes 3–5) in comparison to the control experiment (lane 1). The amount of nicked *form II* produced by compounds **1**–**3** were 28%, 38%, and 25%, respectively. Considering the relative absorption intensity of **1**–**3** at 528 nm (ca. 1:5.7:4.0), the quantum yield in photoinduced DNA damage by C_{60}-PEG **1** was higher, while the damages by C_{70}-PEG **2** and **3** were similar to each other.

DNA damage was significantly enhanced in the presence of NADH (Figure 3a, lanes 6 (87%), 7 (50%), and 8 (57%);

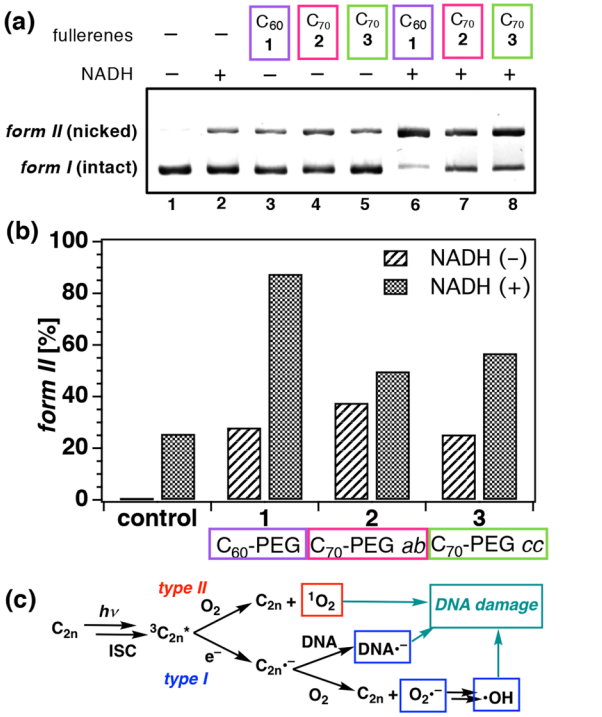

Figure 3. (a) Photoinduced DNA cleavage by C_{60}- and C_{70}-PEG conjugates **1**–**3**, (b) relative formation of nicked *form II*, and (c) expected pathways for DNA damage. DNA: pBR322 supercoiled DNA; right irradiation: green LED (with maximum of 528 nm, 90 lm·W^{-1}) at a distance of 1 cm for 6 h. Lanes 1, 2: control without fullerene; lanes 3, 6: C_{60}-PEG **1**; lanes 4, 7: C_{70}-PEG **2**; lanes 5, 8: C_{70}-PEG **3**. Lanes 1, 3–5: without NADH; lanes 2, 6–8: with NADH (10 mM). Reaction conditions: pBR322:6.25 $\mu g \cdot mL^{-1}$; C_{2n}-PEG: 0.75 mM; NADH: 10 mM; in Tris-HCl buffer (5 mM, pH 8.0, with 0.5 mM EDTA). Electrophoresis: 100 V, 80 min, 1% agarose in TBE buffer (pH 8.3). The figure is inverted form the original image (Figure S20).

Figure 3b) in all C_{2n}-PEG conjugates, presumably due to the stronger reactive species generated via the electron transfer pathway. As described in Figure 3c, there are two possible pathways for DNA damage involving *type I* electron transfer reaction; (1) the generation of radical species of substrate (DNA), or (2) the generation of highly reactive •OH via $O_2^{\bullet-}$. Interestingly, the DNA cleavage by C_{60}-PEG **1** was much more enhanced (3.1 times) by the addition of NADH, resulting in a stronger DNA cleavage than **2** and **3**, which were also enhanced 1.3 and 2.3 times (Figure 3b). The results indicated

https://doi.org/10.1021/jacsau.1c00239
JACS Au 2021, 1, 1601–1611

that in the cases of compounds **1** and **3**, electron-transfer photoreaction proceeded efficiently via either of these pathways, in contrast to compound **2**.

It is known that $^1O_2$ is a key ROS in photoinduced DNA cleavage by *type II* pathway,[37] while the electron transfer to DNA or generation of $O_2^{\bullet-}$ as a precursor of highly reactive •OH are the keys in the DNA cleavage by *type I* pathway (Figure 3c).[38−42] To investigate the current phenomena more clearly, the generations of $^1O_2$ and $O_2^{\bullet-}$ from photoexcited compounds **1**−**3** were estimated by ESR spin-trapping methods. Our aim is not to investigate the mechanism of DNA cleavage but to observe different types of ROS generation from the three fullerene-PEG derivatives.

ESR Measurement of Photoinduced ROS ($^1O_2$ and $O_2^{\bullet-}$) Generation

The photoinduced generation of $^1O_2$ and $O_2^{\bullet-}$ from photoexcited C_{2n}-PEGs **1**−**3** were measured in aqueous media by ESR using corresponding spin-trapping agents. The $^1O_2$, which can be generated via a *type II* energy transfer reaction (Scheme 1), was measured using 4-oxo-TEMP (Figure 4b). Upon irradiation by green LED (528 nm max), the peaks corresponding to 4-oxo-TEMPO were observed in the solution of **1**−**3** in a time-dependent manner (Figures 4a and S22−S25). The relative amount of $^1O_2$ was estimated by double-integration analyses of ESR signals in Figure 4a to show that the generation of $^1O_2$ from C_{70}-PEG **2** was significantly higher than from C_{60}-PEG **1** and C_{70}-PEG **3** (Figure 4b). This result was in good agreement to the results of the photo DNA cleavage assay in the absence of NADH, where stronger DNA damage was observed with **2** in comparison to **1** and **3** (lanes 3−5 in Figure 3a). These results suggested that there was a strong correlation between photo DNA cleavage by **1**−**3** (in the absence of electron donor) and $^1O_2$ generation produced via a *type II* energy transfer mechanism.

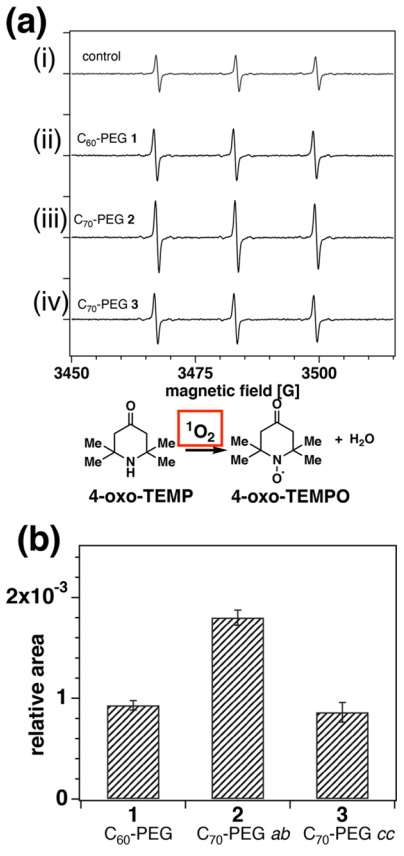

Figure 4. Photoinduced generations of $^1O_2$ from C_{60}-PEG **1** and C_{70}-PEG **2**-**3** in aqueous solutions. (a) ESR spectra of $^1O_2$ adduct of 4-oxo-TEMP in aqueous solution C_{2n}-PEG **1**−**3**, and the scheme for the reaction of $^1O_2$ with a spin trapping reagent, 4-oxo-TEMP. (b) Relative amount of $^1O_2$ generation estimated by double integration of the peaks corresponding to 4-oxo-TEMPO (data are after subtraction of control peak area). C_{2n}-PEG: 40 μM; 4-oxo-TEMP: 80 mM; in 60 mM phosphate buffer (pH 7.0). Photoirradiation conditions: green LED (528 nm, 93 lm·W^{-1}), 4 cm distance, room temperature, 10 min.

Next, the photoinduced $O_2^{\bullet-}$ generation was measured in aqueous solutions of **1**−**3** in the presence of an electron donor (NADH) by ESR using DEPMPO as a spin-trapping reagent (Figure 5). As shown in Figure 5a and b, $O_2^{\bullet-}$ generation was observed from all compounds **1**−**3** in a similar range with slight differences and in a time-dependent manner (Figures S26−S29). As shown in Figure 5c, the observed $O_2^{\bullet-}$ was considered to be a sum of the $O_2^{\bullet-}$ generated through two pathways: (1) direct generation through *type I* electron transfer and (2) reduction of $^1O_2$ first generated via *type II* energy transfer. To exclusively detect only the $O_2^{\bullet-}$ generated via *type I* electron transfer, $O_2^{\bullet-}$ generation was measured in the presence of L-histidine, a $^1O_2$ quencher. As shown in Figure 5b, the amount of $O_2^{\bullet-}$ generated in the presence of L-histidine was significantly decreased in case of C_{70}-PEG **2**, suggesting that the $O_2^{\bullet-}$ generation from compound **2** involved the *type II* energy transfer pathway.

The results clearly indicated that the preferred pathways in the photoinduced reactions of compounds **1**−**3** were different; the photoreaction of C_{70}-PEG **2** primarily involved the *type II* energy transfer mechanism, while C_{60}-PEG **1** and C_{70}-PEG **3** preferred the *type I* electron transfer pathway, providing the different type of ROS generation related to the photoinduced DNA cleavage. To understand the mechanisms of these unexpected differences in these three fullerene derivatives **1**−**3**, experimental investigations were employed: (1) laser flash photolysis to estimate the relative lifetime of the triplet excited states and (2) cyclic voltammetry to obtain the redox potentials and the electron transfer rate of corresponding precursors **4**−**6**. Furthermore, computational calculations were performed to estimate the relative rate for each step in *type II* and *type I* reactions.

Lifetime of the Triplet Excited State

The photophysical properties of **1**−**3** were measured by nanosecond laser flash photolysis. The decay of their triplet-excited states ($^3C_{2n}$*) in water is shown in Figure 6. C_{60}-PEG **1** was excited with 532 nm (20−50 mJ) and C_{70}-PEG **2** and **3** were excited with 355 nm (40−90 mJ), because only minor signals (<1 × 10^{-3} AU) were detected in C_{70} isomers with 532 nm excitation even at laser energies > 150 mJ/pulse. In all three cases and for the majority of wavelengths tested, a double exponential decay was observed, with the faster rate constant (k_{fast}) > 10^6 s^{-1} and the slower (k_{slow}) around 10^5 s^{-1} (Figure 6, Table 1). The observed rate constants were independent of the wavelength. The initial buildup had an apparent rise time of around 10 ns. Given the 5−10 ns width of the laser pulse, the build-up kinetics are too fast to be resolved with our experimental setup.

During the initial absorbance increase, i.e., the buildup of the transient(s) observed, we did not observe substantial fluorescence. It appears that the intersystem crossing (ISC)

https://doi.org/10.1021/jacsau.1c00239
JACS Au 2021, 1, 1601−1611

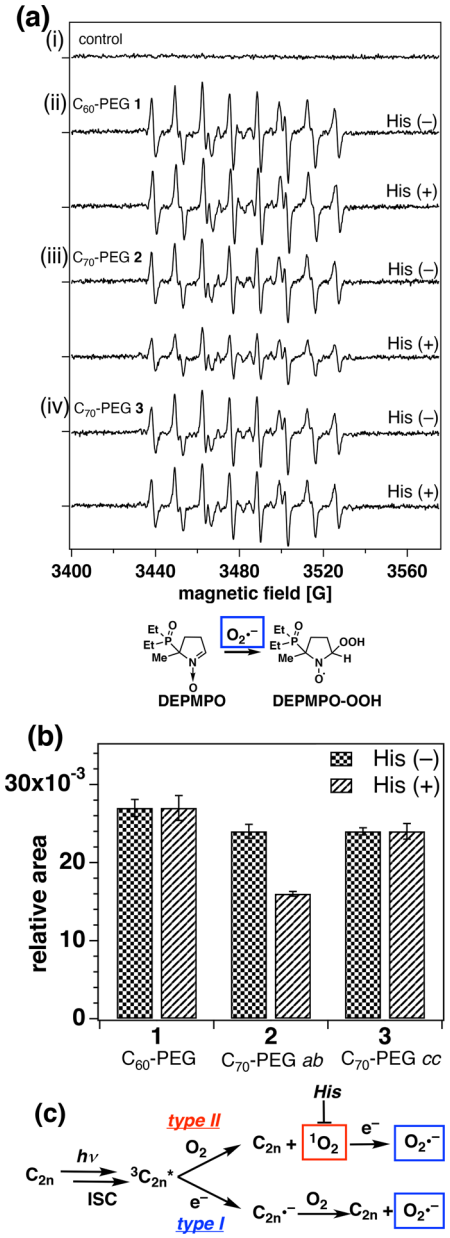

Figure 5. Photoinduced generations of $O_2^{\bullet-}$ from C_{60}-PEG **1** and C_{70}-PEG **2**, **3** in aqueous solutions. (a) ESR spectra of $O_2^{\bullet-}$ adduct of DEPMPO in aqueous solution of C_{2n}-PEG **1**-**3** and corresponding scheme for the reaction of $O_2^{\bullet-}$ with a spin-trapping reagent, DEPMPO. (b) Relative amount of $O_2^{\bullet-}$ generation estimated by double integration of ESR signals in the absence and presence of L-histidine. (c) Scheme for the two possible pathways for $O_2^{\bullet-}$ generations via *type I* or *type II* photoreactions of fullerenes. C_{2n}-PEG: 40 μM; DEPMPO: 113 mM; NADH: 10 mM; DETAPAC: 1 mM; L-histidine: 10 mM; in a mixture of 60 mM phosphate buffer (pH 7.0) and DMSO (20%, v/v). Photoirradiation conditions: green LED (528 nm, 93 lm·W^{-1}), 4 cm distance, room temperature, 3 min.

has a high quantum yield, in line with reported data.[43] The double-exponential decay observed implies either two consecutive or two independent decay processes. The mechanism cannot consist only of two parallel reactions of the same transient species. Guldi reported that water-soluble fullerenes tend to form clusters and that their triplet-to-singlet ($^3C_{2n}$ to $^1C_{2n}$) decay rate was faster than for isolated monomer species.[43] In that original work, surfactants were used to

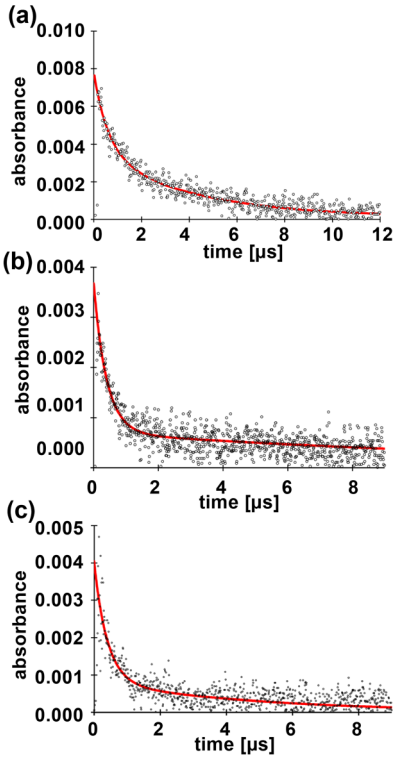

Figure 6. Laser flash photolysis of C_{60}-PEG **1** (a), C_{70}-PEG **2** (b), and C_{70}-PEG **3** (c) in water with double exponential fit for the decay of the excited states. Excitation: 532 nm with energies of 20−30 mJ/pulse for C_{60}-PEG **1**; at 355 nm with energies of 40−70 mJ/pulse for C_{70}-PEG **2**, **3**.

Table 1. Rate Constants and Lifetime of the Triplet Excited-State ($^3C_{2n}$*) of C_{2n}-PEG 1−3 Measured in Water by Laser Flash Photolysis

compd	$k_{slow} \times 10^5$ [s^{-1}]	$k_{fast} \times 10^6$ [s^{-1}]	$^3C_{2n}$* lifetime [μs]
C_{60}-PEG **1**	3.4 ± 0.7	3.6 ± 0.8	~2
C_{70}-PEG **2**	0.9 ± 0.58	2.6 ± 0.9	~7
C_{70}-PEG **3**	1.8 ± 1.20	2.7 ± 0.9	~4

measure the decay rate of monomers, and half-lives of 50−70 μs were found. We find half-lives ($t_{1/2} = \ln(2)/k$) of around 0.2 μs for all fast processes. The slower process has half-lives of 2, 7, and 4 μs for **1**, **2**, and **3**, respectively (Table 1). Within the framework given above, we suspect that the faster process is coupled to the decay of fullerene assembled in micelles, while the slower process is a measure of the decay of fullerene monomers. The latter process was roughly 1 order of magnitude faster than reported by Guldi with similar structures.[43] Additionally, we observed less than 1 order of magnitude lower absorption signals. We do not know if this is related to the fact that Guldi's monomer species were dissolved with surfactants, which would imply that his experiments were carried out with suspensions, not solutions. As the triplets appear to be more stable in organic solvents (150 and 100 μs for C_{60} and C_{70}),[44] a local lipophilic embedding of the fullerenes by surfactants in the original work might have increased the observed half-lives.

More important for our purpose, however, is the longer half-lives of the monomers of **2** and **3** as compared to **1**. A longer half-life increases the probability for intermolecular energy transfer, for example by formation of $^1O_2$. Alternatively, direct

https://doi.org/10.1021/jacsau.1c00239
JACS Au 2021, 1, 1601−1611

excitation of a biomolecule or electron transfer may occur in PDT.

Redox Potential and Electron Transfer Rate

In a *type I* mechanism, the generation of $O_2^{\bullet-}$ from photoexcited fullerenes is directly related to the redox potential of the $C_{2n}/C_{2n}^{\bullet-}$ couple. As the redox properties of **1**−**3** mainly arise from the fullerene core, we investigated the electrochemical properties of the analogous derivatives **4**−**6**, which were more soluble in a mixture of toluene and acetonitrile.[45] Electrochemical studies with these shorter models **4**−**6** in such an organic media yet remain relevant to discuss the overall trend among the electrochemical properties of **1**−**3**, as (i) the fullerene cores are expected to lie on the inside of the micellar structures, having an organic media character, and (ii) the differences in electrochemical properties in such a low dielectric phase is expected to mainly arise from inner-sphere reorganization energy differences, which should not be significantly impacted by the length of the PEG tail.

As shown in Figure 7, all three compounds displayed three reversible reduction processes. As summarized in Table 2, the

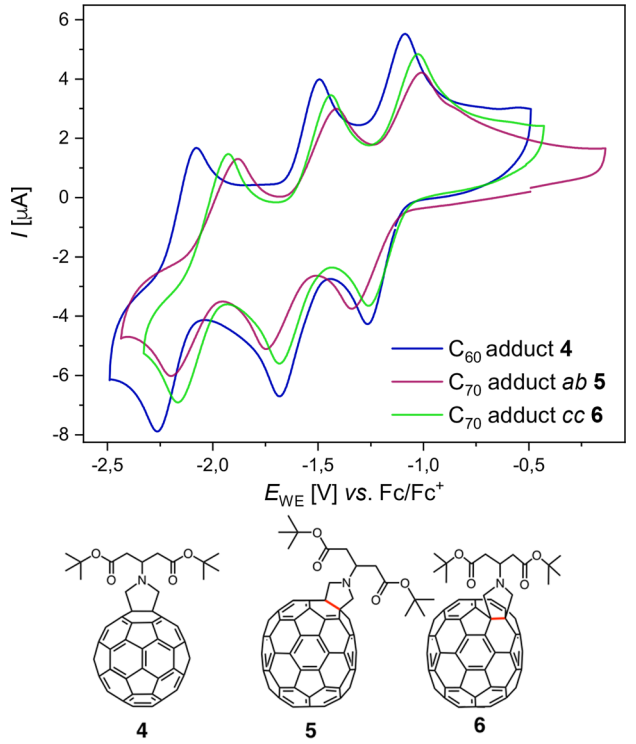

Figure 7. Cyclic voltammograms of C_{2n} Prato adducts **4**-**6** in toluene/acetonitrile (10.4:1) with 0.1 M $TBAPF_6$ at room temperature. The working electrode was a glassy carbon plate, the reference electrode was Ag/AgCl, and the counter electrode was a Pt wire. The scan rate was 100 $mV{\cdot}s^{-1}$. The second scan is shown.

redox potential of the $C_{2n}/C_{2n}^{\bullet-}$ couple is given by the first redox process: among C_{70} analogues, compound **6** appears to be reduced at more modest potentials than compound **5**. From a thermodynamic point of view, this indicates that **6** has a weaker driving force for part 2 of the *type I* mechanism (i.e., the generation of $O_2^{\bullet-}$) than **5** but also that the reduced fullerene species can be generated in part 1 of the mechanism at a lower energetic cost. This latter point is in good agreement with the higher efficiency and stronger DNA damage enhancement observed for **3** vs **2** in the presence of NADH.

Table 2. Redox Potentials and Electron Transfer Rates of Prato Adducts 4−6 Obtained from Cyclic Voltammetry[a]

	reduction potentials [V][b]			
compd	1st	2nd	3rd	electron transfer rate [$cm{\cdot}s^{-1}$]
4	−1.18	−1.59	−2.15	2.6×10^{-5}
5 (ab-[6,6])	−1.18	−1.58	−2.04	1.5×10^{-5}
6 (cc-[6,6])	−1.14	−1.56	−2.05	2.6×10^{-5}

[a]Obtained from Figure 7. [b]In toluene/MeCN (10.4:1) and vs Fc/Fc^+.

The reduction of **3** occurs with a higher driving force than the reduction of **2**. Interestingly, the observation of a comparable amount of $O_2^{\bullet-}$ in the *type I* mechanism with the C_{60} compound **1** (e.g., in the presence of L-histidine, Figure 5b), despite the more negative redox potential of **4** vs **6**, highlights that the driving force of part 2 of the *type I* mechanism has no direct influence of the efficiency of $O_2^{\bullet-}$ generation. Hence, only part 1 of the *type I* mechanism will be considered in the discussion below, in agreement with that step being identified as the rate-determining step by the computational work presented later in text.

However, these thermodynamic considerations do not allow us to fully explain the different behavior of the two C_{70} analogues observed above with respect to the type of mechanism considered. Compound **3** operates mainly via a *type I* mechanism, while compound **2** operates via both *type I* and *II* mechanisms occurring in parallel. To get further insight on the generation of $C_{2n}^{\bullet-}$ species and to determine the type of reaction mechanisms involved, we estimated the kinetics for their formation from the cyclic voltammetry data using the method proposed by Magno and co-workers.[46] The slope of the ψ vs $(\pi n\nu FD/RT)^{-1/2}$ plot gives the heterogeneous rate constant k^0 (Figures S31, S33, and S35), where ψ is defined as

$$\psi = \frac{(-0.6288 + 0.0021X)}{(1 - 0.017X)} \quad (1)$$

where X is the peak-to-peak separation of the anodic and cathodic waves expressed in mV. The electron transfer rate of the C_{70} Prato adduct **5** is ca. 1.8 times slower than the ones of C_{60} adduct **4** and C_{70} adduct **6**. The significantly slower reduction rate of **5**, with respect to **4** and **6**, suggests that the less efficient generation of $O_2^{\bullet-}$ via a *type I* energy transfer reaction observed by ESR in the presence of L-histidine (Figure 5c) for **2**, with respect to **3**, results from the slower kinetics for the reduction of **2**. Interestingly, this correlates well with the longer lifetime of the $^3C_{2n}$* species observed for **2**, with respect to **3**, in agreement with a faster electron transfer rate for **3**, contributing to the consumption of the $^3C_{2n}$* species. These electrochemical studies highlight the interesting predictive potential of simple cyclic voltammetry measurements for the design of efficient fullerene-based compounds for ROS generation. Two favorable scenarios can be identified by electrochemical techniques: for a given C_{2n} compound family, the compound presenting the most cathodic redox potential will possess a higher driving force for the generation of $O_2^{\bullet-}$ via a *type I* energy transfer reaction, while a slow reduction rate will promote the *type II* reaction mechanism.

Computational Studies

To further investigate the mechanism of the ROS generation from C_{2n}-PEG **1**−**3** through the *type I* and the *type II* reactions, computational studies were performed. To make calculations

https://doi.org/10.1021/jacsau.1c00239
JACS Au 2021, 1, 1601−1611

more feasible, NADH and C_{2n}-PEG **1**−**3** were replaced with the model compounds shown in Figure S38. The rate of the studied processes can be estimated using the classical Marcus equation:[47]

$$k_{ET} = \frac{2\pi}{\hbar}|H_{AB}|^2 \frac{1}{(4\pi\lambda_t k_b T)^{1/2}} \exp\left(\frac{-(\lambda_t + \Delta G)^2}{4\lambda_t k_b T}\right) \quad (2)$$

where $|H_{AB}|$ is the electronic matrix element describing the electronic coupling between the electronic states of the reactants and the products, ΔG is the Gibbs energy, and λ_t is the total reorganization energy. λ_t is the sum of two components, the internal reorganization energy (λ_i) and the external reorganization energy (λ_s). $|H_{AB}|$ is known to be quite sensitive to the mutual orientation of the donor and acceptor sites and this dependence makes $|H_{AB}|$ calculation problematic for the studied systems, which are quite flexible. When comparing reaction rates, we have assumed similar $|H_{AB}|$ for species **1**-**3**. For all considered processes, the limit between the normal and the inverted Marcus regime, and consequently the highest predicted rate, is reached with ΔG (Gibbs energy) = $-\lambda_t$ (reorganization energy). Analyses of ($\Delta G + \lambda_t$) and relative rates for the *type II* reaction are summarized in Table 3. Table S1 contains the values of ΔG and λ_t. The Gibbs energy of the $^3\Sigma_g^-$ ($^3O_2$) to $^1\Delta_g$ ($^1O_2$) process was taken from experiments.[48]

Table 3. Sum of Gibbs Energies and Total Reorganization Energies ($\Delta G + \lambda_t$) and Relative Rates for the *Type II* Reaction

systems	*type II*	
	($\Delta G+\lambda_t$) [eV]	relative rate
1/**4** (model)	−0.754	slow
2/**5** (model)	−0.368	medium/fast
3/**6** (model)	−0.297	medium/fast

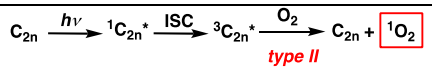

For all the C_{2n}-PEG models, the *type II* reaction occurs in the inverted Marcus regime ($|\Delta G| > \lambda_t$). By considering that the ISC and the $^1O_2$ generation process are linked reactions, in which the product of the first reaction becomes the substrate of the second reaction, the rate of the whole process should be determined by the rate of the slowest reaction. The similar computed ($\Delta G + \lambda_t$) values for the *type II* mechanism for **2** and **3** further confirms the conclusions of the electro- and photochemical experiments: the *type II* mechanism presents a comparable driving force and kinetics for both compounds, but it occurs in competition with the *type I* mechanism for both. As the *type I* mechanism is disfavored by the slow electron transfer rate for **2**, this results in the longer lifetime of the $^3C_{2n}$* state for **2**, as observed in the photophysical data and the increased occurrence of the *type II* mechanism.

The ($\Delta G + \lambda_t$) values for the *type I* reaction mechanism are gathered in Table 4. The *type I* reaction involves also the initial ISC, and then it can be divided into two parts (parts 1 and 2, shown in the Scheme of Table 4). To better investigate the role of each process in the determination of the rate of the generation of $O_2^{\bullet-}$, we have computed the ($\Delta G + \lambda_t$) and relative rates for parts 1 and 2 of the *type I* reaction (Table 4).

Table 4. Sum of Gibbs Energies and Total Reorganization Energies ($\Delta G + \lambda_t$) and Relative Rates for the *Type I* Reaction

systems	*type I*, part 1		*type I*, part 2	
	($\Delta G+\lambda_t$) [eV]	relative rate	($\Delta G+\lambda_t$) [eV]	relative rate
1/**4** (model)	0.132	fast	0.523	medium
2/**5** (model)	0.379	medium	0.540	medium
3/**6** (model)	0.416	slow/medium	0.526	medium

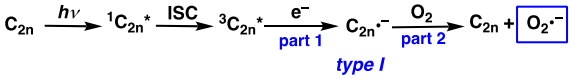

For all the C_{2n}-PEG models, parts 1 and 2 of the *type I* reaction occur in the normal Marcus regime ($|\Delta G| < \lambda_t$). Hence, the calculated higher reduction rate of $^3C_{2n}$ (part 1) observed for **2** vs **3** is in agreement with the more negative redox potential determined for **2** vs **3**. The faster kinetics of compound **1** determined here results from the lower reorganization energy λ_t of the C_{60} compound, with respect to the C_{70} ones (Table S1). On the other hand, the final generation of $O_2^{\bullet-}$ in part 2 show similar rates for all species **1**−**3**. The slightly more efficient generation of $O_2^{\bullet-}$ by C_{60}-PEG **1** measured in the ESR experiments (Figure 5), in spite of its lower absorbance, suggests that part 1 is the rate-limiting step of *type I* reaction ($k_{typeI,\ part1} < k_{typeI,\ part2}$), in agreement with the electrochemical data.

CONCLUSION

The well-defined water-soluble C_{60}-PEG and C_{70}-PEG conjugates **1**−**3** were prepared and tested for photoinduced DNA damage and ROS generation under visible light irradiation. The generation of $^1O_2$ and photo DNA cleavage via the *type II* energy transfer pathway was higher in C_{70}-PEG **2** with the *ab*-[6,6]-addition site. Efficient generation of $^1O_2$ from C_{70}-PEG **2** was explained by (1) the higher absorption intensity at 528 nm and (2) the longer lifetime of its triplet excited state, as suggested by laser flash photolysis measurements. The DNA damage in the presence of electron donor via the *type I* electron transfer pathway was much higher in C_{60}-PEG **1** despite its lower absorption intensity. The $O_2^{\bullet-}$ generation, which is partially related to the DNA damage, was observed to be higher in C_{60}-PEG **1** and C_{70}-PEG **3**, especially in the presence of L-histidine. By the cyclic voltammetry measurements, C_{60}-PEG **1** and C_{70}-PEG **3** were characterized by the same faster electron transfer rates, providing more generation of $O_2^{\bullet-}$ probably due to its larger impurity diffusion enhancement of interdiffusion (IDEI). Computational results based on the Marcus equation confirm the experimental findings showing that the *type II* energy transfer reaction occurs in the inverted Marcus regime whereas the *type I* electron transfer reaction proceeds in the normal Marcus regime.

This work showed, for the first time, a clearly different preference of ROS generation from the photoexcited C_{60}-PEG **1** and C_{70}-PEG **3**, generating more $O_2^{\bullet-}$, from the photoexcited C_{70}-PEG **2**, generating more $^1O_2$, in water. The pathway disparity was dependent on the fullerene core (C_{60} or C_{70}) and functionalization pattern. The result provides the guidelines for important parameters to consider and optimize

https://doi.org/10.1021/jacsau.1c00239
JACS Au 2021, 1, 1601−1611

(excited states lifetime, redox potential, electron transfer rate) for the preparation of efficient PDT-PSs. Importantly, but not part of this investigation, *type I* reaction part 1 represents not only a reduction of $^3C_{2n}$* but also an oxidation of a nonspecified reaction partner. To understand better the mechanism of DNA damage by ROS generated from photoexcited fullerenes, further investigations using substrates such as guanine or 8-oxoguanine are in progress.

■ ASSOCIATED CONTENT

Supporting Information

. The Supporting Information is available free of charge on the ACS Publications Web site. The Supporting Information is available free of charge at https://pubs.acs.org/doi/10.1021/jacsau.1c00239.

> Detail of the preparation of C_{70}-PEG conjugates with corresponding spectral data, DLS data, experimental methods for DNA cleavage tests and ESR spin-trapping methods; full computational details, full reference, model compounds, Cartesian coordinates of all optimized species; values of Gibbs energies ΔG and total reorganization energy λ_t computed in water for systems **1**−**3** (PDF)

■ AUTHOR INFORMATION

Corresponding Authors

Yoko Yamakoshi − *Laboratorium für Organische Chemie, ETH Zürich, CH-8093 Zürich, Switzerland;* orcid.org/0000-0001-8466-0118; Email: yamakoshi@org.chem.ethz.ch

Victor Mougel − *Laboratorium für Anorganische Chemie, ETH Zürich, CH-8093 Zürich, Switzerland;* Email: mougel@inorg.chem.ethz.ch

Miquel Solà − *Institut de Química Computacional i Catàlisi (IQCC) and Departament de Química, Universitat de Girona, 17003 Girona, Catalonia, Spain;* orcid.org/0000-0002-1917-7450; Email: miquel.sola@udg.edu

Authors

Korinne Liosi − *Laboratorium für Organische Chemie, ETH Zürich, CH-8093 Zürich, Switzerland*

Anton J. Stasyuk − *Institut de Química Computacional i Catàlisi (IQCC) and Departament de Química, Universitat de Girona, 17003 Girona, Catalonia, Spain;* orcid.org/0000-0003-1466-8207

Fabio Masero − *Laboratorium für Anorganische Chemie, ETH Zürich, CH-8093 Zürich, Switzerland*

Alexander A. Voityuk − *Institut de Química Computacional i Catàlisi (IQCC) and Departament de Química, Universitat de Girona, 17003 Girona, Catalonia, Spain; Institució Catalana de Recerca i Estudis Avancats (ICREA), 08010 Barcelona, Catalonia, Spain;* orcid.org/0000-0001-6620-4362

Thomas Nauser − *Laboratorium für Anorganische Chemie, ETH Zürich, CH-8093 Zürich, Switzerland;* orcid.org/0000-0002-5692-5737

Complete contact information is available at: https://pubs.acs.org/10.1021/jacsau.1c00239

Author Contributions

The manuscript was written through contributions of all authors. All authors have given approval to the final version of the manuscript.

Notes

The authors declare no competing financial interest.

■ ACKNOWLEDGMENTS

The authors thank Dr. Sologubenko in ScopeM at ETH for her help in STEM measurements and analyses. The authors thank Prof. Hilvert in ETH for the access to the transilluminator. The authors thank Prof. Morbidelli and Prof. Arosio in ETH for their help in DLS analysis. The ScopeM of ETH, the NMR service, and MoBiAS in the LOC at ETH are acknowledged for their help in measurements. This study was supported in part by the Swiss National Foundation (200021_156097, 205321_17318, Y.Y.), the ETH Research Grant (ETH-21 15-2, ETH-25 11-1, Y.Y.), the Spanish MINECO (Network RED2018-102815-T, projects CTQ2017-85341-P and PID2020-113711GB-I00, and Juan de la Cierva contract IJC2019-039846-I to A.J.S.) and the Catalan DIUE (2017SGR39).

■ REFERENCES

(1) Tokuyama, H.; Yamago, S.; Nakamura, E.; Shiraki, T.; Sugiura, Y. Photoinduced Biochemical-Activity of Fullerene Carboxylic-Acid. *J. Am. Chem. Soc.* **1993**, *115* (17), 7918−7919.

(2) Nakamura, E.; Isobe, H. Functionalized Fullerenes in Water. The First 10 Years of Their Chemistry, Biology, and Nanoscience. *Acc. Chem. Res.* **2003**, *36* (11), 807−815.

(3) Castro, E.; Hernandez Garcia, A.; Zavala, G.; Echegoyen, L. Fullerenes in Biology and Medicine. *J. Mater. Chem. B* **2017**, *5* (32), 6523−6535.

(4) Arbogast, J. W.; Darmanyan, A. P.; Foote, C. S.; Rubin, Y.; Diederich, F. N.; Alvarez, M. M.; Anz, S. J.; Whetten, R. L. Photophysical Properties of C_{60}. *J. Phys. Chem.* **1991**, *95* (1), 11−12.

(5) Arbogast, J. W.; Foote, C. S. Photophysical Properties of C_{70}. *J. Am. Chem. Soc.* **1991**, *113* (23), 8886−8889.

(6) Nagano, T.; Arakane, K.; Ryu, A.; Masunaga, T.; Shinmoto, K.; Mashiko, S.; Hirobe, M. Comparison of Singlet Oxygen Production Efficiency of C_{60} with Other Photosensitizers, Based on 1268-nm Emission. *Chem. Pharm. Bull.* **1994**, *42* (11), 2291−2294.

(7) Fraelich, M. R.; Weisman, R. B. Triplet-States of C_{60} and C_{70} in Solution - Long Intrinsic Lifetimes and Energy Pooling. *J. Phys. Chem.* **1993**, *97* (43), 11145−11147.

(8) Wasielewski, M. R.; O'Neil, M. P.; Lykke, K. R.; Pellin, M. J.; Gruen, D. M. Triplet-States of Fullerenes C_{60} and C_{70} - Electron-Paramagnetic Resonance-Spectra, Photophysics, and Electronic-Structures. *J. Am. Chem. Soc.* **1991**, *113* (7), 2774−2776.

(9) Kumar, R.; Gleissner, E. H.; Tiu, E. G. V.; Yamakoshi, Y. C_{70} as a Photocatalyst for Oxidation of Secondary Benzylamines to Imines. *Org. Lett.* **2016**, *18* (2), 184−187.

(10) Krusic, P. J.; Wasserman, E.; Parkinson, B. A.; Malone, B.; Holler, E. R.; Keizer, P. N.; Morton, J. R.; Preston, K. F. Electron-Spin-Resonance Study of the Radical Reactivity of C_{60}. *J. Am. Chem. Soc.* **1991**, *113* (16), 6274−6275.

(11) Arbogast, J. W.; Foote, C. S.; Kao, M. Electron-Transfer to Triplet C_{60}. *J. Am. Chem. Soc.* **1992**, *114* (6), 2277−2279.

(12) Yamakoshi, Y.; Sueyoshi, S.; Fukuhara, K.; Miyata, N.; et al. •OH and $O_2^{-\bullet}$ Generation in Aqueous C_{60} and C_{70} Solutions by Photoirradiation: An EPR study. *J. Am. Chem. Soc.* **1998**, *120* (47), 12363−12364.

(13) Yamakoshi, Y.; Umezawa, N.; Ryu, A.; Arakane, K.; Miyata, N.; Goda, Y.; Masumizu, T.; Nagano, T. Active Oxygen Species Generated From Photoexcited Fullerene (C_{60}) as Potential

Medicines: $O_2^{-\bullet}$ *versus* $^1O_2$. *J. Am. Chem. Soc.* **2003**, *125* (42), 12803−12809.
(14) Yamakoshi, Y.; Aroua, S.; Nguyen, T. M.; Iwamoto, Y.; Ohnishi, T. Water-Soluble Fullerene Materials for Bioapplications: Photoinduced Reactive Oxygen Species Generation. *Faraday Discuss.* **2014**, *173*, 287−296.
(15) Oriana, S.; Aroua, S.; Sollner, J. O.; Ma, X. J.; Iwamoto, Y.; Yamakoshi, Y. Water-soluble C_{60}- and C_{70}-PVP Polymers for Biomaterials with Efficient $^1O_2$ Generation. *Chem. Commun.* **2013**, *49* (81), 9302−9304.
(16) Iwamoto, Y.; Yamakoshi, Y. A Highly Water-soluble C_{60}-NVP Copolymer: a Potential Material for Photodynamic Therapy. *Chem. Commun.* **2006**, No. 46, 4805−4807.
(17) Sperandio, F. F.; Sharma, S. K.; Wang, M.; Jeon, S.; Huang, Y. Y.; Dai, T. H.; Nayka, S.; de Sousa, S. C. O. M.; Chiang, L. Y.; Hamblin, M. R. Photoinduced Electron-Transfer Mechanisms for Radical-Enhanced Photodynamic Therapy Mediated by Water-Soluble Decacationic C_{70} and $C_{84}O_2$ Fullerene Derivatives. *Nanomedicine* **2013**, *9* (4), 570−579.
(18) Huang, L. Y.; Wang, M.; Dai, T. H.; Sperandio, F. F.; Huang, Y. Y.; Xuan, Y.; Chiang, L. Y.; Hamblin, M. R. Antimicrobial Photodynamic Therapy with Decacationic Monoadducts and Bisadducts of [70] Fullerene: *in vitro* and *in vivo* Studies. *Nanomedicine* **2014**, *9* (2), 253−266.
(19) Herrmann, A.; Diederich, F.; Thilgen, C.; Termeer, H. U.; Muller, W. H. Chemistry of the Higher Fullerenes - Preparative Isolation of C_{76} by HPLC and Synthesis, Separation, and Characterization of Diels-Alder Monoadducts of C_{70} and C_{76}. *Helv. Chim. Acta* **1994**, *77* (7), 1689−1706.
(20) Liosi, K.; Romero-Rivera, A.; Semivrazhskaya, O.; Caniglia, C. D.; Garcia-Borras, M.; Trapp, N.; Osuna, S.; Yamakoshi, Y. Site-Selectivity of Prato Additions to C_{70}: Experimental and Theoretical Studies of a New Thermodynamic Product at the dd-[5,6]-Junction. *Org. Lett.* **2019**, *21* (13), 5162−5166.
(21) Mestres, J.; Duran, M.; Sola, M. Theoretical Study of Diels-Alder Cycloadditions of Butadiene to C_{70}. An Insight into the Chemical Reactivity of C_{70} as Compared to C_{60}. *J. Phys. Chem.* **1996**, *100* (18), 7449−7454.
(22) Dallas, P.; Rogers, G.; Reid, B.; Taylor, R. A.; Shinohara, H.; Briggs, G. A. D.; Porfyrakis, K. Charge Separated States and Singlet Oxygen Generation of Mono and Bis Adducts of C_{60} and C_{70}. *Chem. Phys.* **2016**, *465*, 28−39.
(23) Umeyama, T.; Miyata, T.; Jakowetz, A. C.; Shibata, S.; Kurotobi, K.; Higashino, T.; Koganezawa, T.; Tsujimoto, M.; Gelinas, S.; Matsuda, W.; Seki, S.; Friend, R. H.; Imahori, H. Regioisomer Effects of [70]Fullerene Mono-Adduct Acceptors in Bulk Heterojunction Polymer Solar Cells. *Chem. Sci.* **2017**, *8* (1), 181−188.
(24) Aroua, S.; Tiu, E. G. V.; Ishikawa, T.; Yamakoshi, Y. Well-Defined Amphiphilic C_{60}-PEG Conjugates: Water-Soluble and Thermoresponsive Materials. *Helv. Chim. Acta* **2016**, *99* (10), 805−813.
(25) Aroua, S.; Schweizer, W. B.; Yamakoshi, Y. C_{60} Pyrrolidine Bis-Carboxylic Acid Derivative as a Versatile Precursor for Biocompatible Fullerenes. *Org. Lett.* **2014**, *16* (6), 1688−1691.
(26) Yanai, T.; Tew, D. P.; Handy, N. C. A New Hybrid Exchange-Correlation Functional Using the Coulomb-Attenuating Method (CAM-B3LYP). *Chem. Phys. Lett.* **2004**, *393* (1−3), 51−57.
(27) Weigend, F.; Ahlrichs, R. Balanced Basis Sets of Split Valence, Triple Zeta Valence and Quadruple Zeta Valence Quality for H to Rn: Design and Assessment of Accuracy. *Phys. Chem. Chem. Phys.* **2005**, *7* (18), 3297−3305.
(28) Grimme, S.; Antony, J.; Ehrlich, S.; Krieg, H. A Consistent and Accurate *Ab Initio* Parametrization of Density Functional Dispersion Correction (DFT-D) for the 94 Elements H-Pu. *J. Chem. Phys.* **2010**, *132* (15), 154104.
(29) Grimme, S.; Ehrlich, S.; Goerigk, L. Effect of the Damping Function in Dispersion Corrected Density Functional Theory. *J. Comput. Chem.* **2011**, *32* (7), 1456−1465.
(30) Osuna, S.; Swart, M.; Sola, M. Dispersion Corrections Essential for the Study of Chemical Reactivity in Fullerenes. *J. Phys. Chem. A* **2011**, *115* (15), 3491−3496.
(31) Hirata, S.; Head-Gordon, M. Time-Dependent Density Functional Theory Within the Tamm-Dancoff Approximation. *Chem. Phys. Lett.* **1999**, *314* (3−4), 291−299.
(32) Besalu-Sala, P.; Voityuk, A. A.; Luis, J. M.; Sola, M. Evaluation of Charge-Transfer Rates in Fullerene-Based Donor-Acceptor Dyads with Different Density Functional Approximations. *Phys. Chem. Chem. Phys.* **2021**, *23* (9), 5376−5384.
(33) Voityuk, A. A.; Vyboishchikov, S. F. A Simple COSMO-Based Method for Calculation of Hydration Energies of Neutral Molecules. *Phys. Chem. Chem. Phys.* **2019**, *21* (34), 18706−18713.
(34) Voityuk, A. A.; Vyboishchikov, S. F. Fast and Accurate Calculation of Hydration Energies of Molecules and Ions. *Phys. Chem. Chem. Phys.* **2020**, *22* (26), 14591−14598.
(35) Frisch, M. J.; Trucks, G. W.; Schlegel, H. B.; Scuseria, G. E.; Robb, M. A.; Cheeseman, J. R.; Scalmani, G.; Barone, V.; Petersson, G. A.; Nakatsuji, H.; Li, X.; Caricato, M.; Marenich, A. V.; Bloino, J.; Janesko, B. G.; Gomperts, R.; Mennucci, B.; Hratchian, H. P.; Ortiz, J. V.; Izmaylov, A. F.; Sonnenberg, J. L.; Williams-Young, D.; Ding, F.; Lipparini, F.; Egidi, F.; Goings, J.; Peng, B.; Petrone, A.; Henderson, T.; Ranasinghe, D.; Zakrzewski, V. G.; Gao, J.; Rega, N.; Zheng, G.; Liang, W.; Hada, M.; Ehara, M.; Toyota, K.; Fukuda, R.; Hasegawa, J.; Ishida, M.; Nakajima, T.; Honda, Y.; Kitao, O.; Nakai, H.; Vreven, T.; Throssell, K.; Montgomery, J. A., Jr.; Peralta, J. E.; Ogliaro, F.; Bearpark, M. J.; Heyd, J. J.; Brothers, E. N.; Kudin, K. N.; Staroverov, V. N.; Keith, T. A.; Kobayashi, R.; Normand, J.; Raghavachari, K.; Rendell, A. P.; Burant, J. C.; Iyengar, S. S.; Tomasi, J.; Cossi, M.; Millam, J. M.; Klene, M.; Adamo, C.; Cammi, R.; Ochterski, J. W.; Martin, R. L.; Morokuma, K.; Farkas, O.; Foresman, J. B.; Fox, D. J. *Gaussian 16*, rev. A.03; Gaussian, Inc.: Wallingford, CT, 2016.
(36) In our previous study, it was shown that compound **1** forms micelles by the observation of a concentration-dependent change in surface tension.
(37) Di Mascio, P.; Martinez, G. R.; Miyamoto, S.; Ronsein, G. E.; Medeiros, M. H. G.; Cadet, J. Singlet Molecular Oxygen Reactions with Nucleic Acids, Lipids, and Proteins. *Chem. Rev.* **2019**, *119* (3), 2043−2086.
(38) Baptista, M. S.; Cadet, J.; Di Mascio, P.; Ghogare, A. A.; Greer, A.; Hamblin, M. R.; Lorente, C.; Nunez, S. C.; Ribeiro, M. S.; Thomas, A. H.; Vignoni, M.; Yoshimura, T. M. Type I and Type II Photosensitized Oxidation Reactions: Guidelines and Mechanistic Pathways. *Photochem. Photobiol.* **2017**, *93* (4), 912−919.
(39) Cadet, J.; Davies, K. J. A.; Medeiros, M. H. G.; Di Mascio, P.; Wagner, J. R. Formation and Repair of Oxidatively Generated Damage in Cellular DNA. *Free Radical Biol. Med.* **2017**, *107*, 13−34.
(40) Cadet, J.; Douki, T.; Ravanat, J. L. Oxidatively Generated Damage to the Guanine Moiety of DNA: Mechanistic Aspects and Formation in Cells. *Acc. Chem. Res.* **2008**, *41* (8), 1075−1083.
(41) Wagner, J. R.; Cadet, J. Oxidation Reactions of Cytosine DNA Components by Hydroxyl Radical and One-Electron Oxidants in Aerated Aqueous Solutions. *Acc. Chem. Res.* **2010**, *43* (4), 564−571.
(42) Rokhlenko, Y.; Cadet, J.; Geacintov, N. E.; Shafirovich, V. Mechanistic Aspects of Hydration of Guanine Radical Cations in DNA. *J. Am. Chem. Soc.* **2014**, *136* (16), 5956−5962.
(43) Guldi, D. M. Capped fullerenes: Stabilization of Water-Soluble Fullerene Monomers as Studied by Flash Photolysis and Pulse Radiolysis. *J. Phys. Chem. A* **1997**, *101* (21), 3895−3900.
(44) Dimitrijevic, N. M.; Kamat, P. V. Triplet Excited-State Behavior of Fullerenes - Pulse-Radiolysis and Laser Flash-Photolysis of C_{60} and C_{70} in Benzene. *J. Phys. Chem.* **1992**, *96* (12), 4811−4814.
(45) Since compounds **1**−**3** are known to form micelle-type aggregation in water and may cause the problem in the measurement of cyclic voltammetry on the surface of electrode, precursor Prato adducts **4**−**6** were used in $CHCl_3$ solutions.
(46) Lavagnini, I.; Antiochia, R.; Magno, F. An Extended Method for the Practical Evaluation of the Standard Rate Constant from Cyclic Voltammetric Data. *Electroanalysis* **2004**, *16* (6), 505−506.

https://doi.org/10.1021/jacsau.1c00239
JACS Au 2021, 1, 1601−1611

(47) Marcus, R. A.; Sutin, N. Electron Transfers in Chemistry and Biology. *Biochim. Biophys. Acta, Rev. Bioenerg.* **1985**, *811* (3), 265–322.
(48) Schweitzer, C.; Schmidt, R. Physical Mechanisms of Generation and Deactivation of Singlet Oxygen. *Chem. Rev.* **2003**, *103* (5), 1685–757.

https://doi.org/10.1021/jacsau.1c00239
JACS Au 2021, 1, 1601–1611